

Supercapacitive Properties of Hydrothermally Synthesized Co_3O_4 Nanostructures

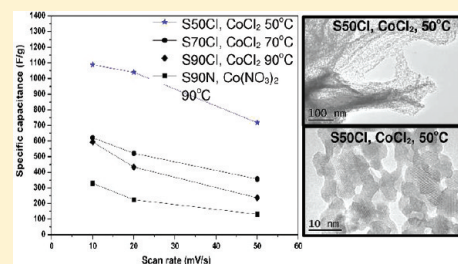
Huatao Wang,^{†,‡,§} Li Zhang,^{*,†,‡} Xuehai Tan,^{†,‡} Chris M.B. Holt,^{†,‡} Benjamin Zahiri,^{†,‡} Brian C. Olsen,^{†,‡} and David Mitlin^{*,†,‡}

[†]Department of Chemical and Materials Engineering, University of Alberta, Edmonton, AB, T6G 2 V4, Canada

[‡]National Institute for Nanotechnology, 11421 Saskatchewan Drive, Edmonton, AB, T6G 2M9, Canada

[§]School of Materials Science and Engineering, Harbin Institute of Technology at Weihai, Weihai, Shandong, 264209, People's Republic of China

ABSTRACT: A hydrothermal process was employed to create a variety of Co_3O_4 nanostructures. We demonstrate that nominally minor differences in the synthesis temperature (50, 70, or 90 °C) yield profound variations in the oxide microstructure, with lath-like, necklace-like and net-like morphologies of different scales resulting. This in turn resulted in significant variations in the supercapacitive performance that ranged from mediocre to superb. Specifically, the mesoporous net-like Co_3O_4 nanostructures that were synthesized at 50 °C exhibited very favorable electrochemical properties: The net-like Co_3O_4 had a specific capacitance of 1090 F/g at a mass loading of 1.4 mg/cm². At this high mass loading, such performance has not been previously reported. SEM and TEM analysis of these samples revealed an interconnected array of sub-10 nm crystallites interspersed with a high volume fraction of similar scale pores. The poorer performing microstructures were both coarser and much less porous.



1. INTRODUCTION

Supercapacitors are energy storage devices that can supply extremely high but transient power output. They are both being utilized and considered for numerous power source applications such as auxiliary power sources for hybrid electric vehicles and short-term power sources for mobile electronic devices. Depending on the charge-storage mode, supercapacitors are generally classified into three major types: carbon- or polymer-based Electric Double-Layer Capacitor (EDLC) and faradaic pseudocapacitor. The capacitance in the former is largely (not entirely) electrostatic in origin, arising from charge separation at the interface of the high specific-area electrode and electrolyte. Activated, mesoporous and carbide-derived carbons, polymer-based textiles and fabrics, and carbon nanotubes and graphene have all been widely investigated for EDLC applications, e.g., refs 1–6.

Pseudocapacitors rely on reversible surface redox reactions to store charge. Materials utilized for pseudocapacitors primarily consist of either bulk oxides or nitrides that have been oxidized on their surface.^{7–11} For pseudocapacitors, most of the charge is stored through fast and reversible redox reactions at the electrode surface and produces what is called pseudocapacitance. In the past decade, a novel class of materials, including some inorganic compounds (transition metal oxides or hydrates, such as hydrous RuO_2 ,¹² MnO_2 ,¹³ $\alpha\text{-MoO}_3$,¹⁴ Bi_2O_3 ,¹⁵ $\text{Co}(\text{OH})_2$,¹⁶ and so on) with various nanoscale microstructures, have been proposed as potential candidates for application in electrodes of supercapacitors. Ruthenium oxide and manganese oxide are widely investigated. Hydrous RuO_2 exhibits remarkably high specific capacitance and excellent reversibility because of the

ideal solid-state pseudofaradaic reaction. However, RuO_2 commercial applications are limited due to its high cost, low porosity and toxic nature. MnO_2 is considered to be another promising material for supercapacitors due to its high energy density, low cost, environmental friendliness, and natural abundance. However, owing to its poor electrical conductivity and poor cyclic stability, manganese oxide is still limited to potential applications.

Among the metal oxides, cobalt oxide (Co_3O_4) has been reported as a promising electrode material for supercapacitors and lithium-ion batteries due to its excellent electrochemical performance.^{17–20} Recently, needle-like Co_3O_4 nanorods with a specific capacitance of 111 F/g were synthesized in a solvothermal system.²¹ Authors prepared Co_3O_4 aerogels with an epoxide synthetic route, having excellent supercapacitive properties of ~625 F/g at a high mass loading of 1 mg/cm².²² That study was considered a significant advancement in the field due to the high mass loading that was achieved. Freely standing Co_3O_4 nanowire arrays with a specific capacitance of 746 F/g were prepared via a simple template-free way.²³ Cobalt oxide nanostructures such as nanoparticles,²⁴ nanorods,²⁵ nanowires,²⁶ nanobelts,²⁷ nanotubes,²⁸ nanosheets,²⁹ nanocubes,³⁰ nanoneedles,³¹ nanocolumns,³² nanodiscs,³³ nanospheres,³⁴ and nanoboxes,³⁵ and macroporous platelets³⁶ have been synthesized via hydrothermal, solvothermal, thermal oxidation, combustion and template methods.

Received: May 27, 2011

Revised: July 19, 2011

Published: July 20, 2011

Polymer coated Co_3O_4 and graphene nanocomposites were also synthesized in the recent years.^{37,38}

A key target for oxide-based supercapacitor research is to achieve an ever-increasing mass loading without sacrificing farads per gram performance. Furthermore, it would be attractive if the electrochemically active materials were grown directly on the current collector without the use of any supplementary conducting material or binder. In this work, large-scale Co_3O_4 nanostructure arrays on Ni foam substrates were prepared via a hydrothermal process and directly employed as supercapacitive electrodes. Relative to previous studies, we were able to achieve a unique combination of exceptional supercapacitive performance ($>1000 \text{ F/g}$) and a very high mass loading (1.4 mg/cm^2). We also demonstrate that seemingly small variations in the synthesis methodology can yield profound changes in the microstructure of the resultant oxide and hence in the capacitive performance.

2. EXPERIMENTAL SECTION

2.1. Materials Synthesis. In this work, we utilize a hydrothermal synthesis approach to create a variety of nanostructures. The methodology utilized is analogous to that employed in refs 39–41 though with growth temperatures, aging times, and molar ratios that differ from these previous studies. All chemicals were analytical grade reagent purchased from Sigma-Aldrich. The cobalt oxide nanostructures were achieved via a hydrothermal

solution procedure followed by calcining in air. The process can be broadly subdivided into two sequential steps: Cobalt-hydroxide-carbonate intermediate nanostructures are first grown on the surface of substrates at $50\text{--}90^\circ\text{C}$ in a solution of cobalt precursor and urea. Second, these intermediate hydroxide-carbonate nanostructures are converted into the Co_3O_4 nanostructures via the calcination process. The general sample morphology achieved during step one is maintained after calcination, though with the introduction of various levels of mesoporosity.

Cobalt salt solutions were taken as the cobalt precursors, and urea $[(\text{NH}_2)_2\text{CO}]$ was used as the precipitant. In our experiments, $\text{CoCl}_2 \cdot 6\text{H}_2\text{O}$, $\text{Co}(\text{NO}_3)_2 \cdot 6\text{H}_2\text{O}$, and $\text{Co}(\text{CH}_3\text{COO})_2 \cdot 4\text{H}_2\text{O}$ have been tried, but only $\text{CoCl}_2 \cdot 6\text{H}_2\text{O}$ and $\text{Co}(\text{NO}_3)_2 \cdot 6\text{H}_2\text{O}$ could be used to grow large-scale arrays of cobalt-based intermediate nanostructures. In a typical run, $0.60 \text{ g CoCl}_2 \cdot 6\text{H}_2\text{O}$ and 1.89 g urea are dissolved in 8.0 mL of Milli-Q water to form a dark-red homogeneous solution. The solution is then transferred to a common 50 mL polypropylene container with pieces of clean substrates at the bottom. The container is sealed and heated to $50\text{--}90^\circ\text{C}$ for $1\text{--}24 \text{ h}$. After the container is cooled to room temperature a pink precipitate is found to grow on the substrates. The precipitate covered substrates are then washed three times with Milli-Q water, and dried naturally. At last, the dried product is annealed at $170\text{--}300^\circ\text{C}$ for 4 h . The pink precipitate is converted into a black one, while retaining its excellent adhesion to the support. The support utilized for all electrochemical experiments was nickel foam.

In our experiments, the designation of S90N, S90Cl, S70Cl, and S50Cl refers to the samples grown at 90°C using $\text{Co}(\text{NO}_3)_2 \cdot 6\text{H}_2\text{O}$, and the samples grown at $90, 70$, and 50°C using $\text{CoCl}_2 \cdot 6\text{H}_2\text{O}$, respectively. Table 1 provides the shorthand designations used throughout this work along with the pertinent processing conditions. A high precision balance, with 0.01 mg accuracy, was used to calculate the mass loadings, with the weight of the postcalcination Co_3O_4 being quoted.

Table 1. Sample Designation As Related to Growth Conditions

sample shorthand	growth temperature, $^\circ\text{C}$	cobalt precursor
S50Cl	50	$\text{CoCl}_2 \cdot 6\text{H}_2\text{O}$
S70Cl	70	$\text{CoCl}_2 \cdot 6\text{H}_2\text{O}$
S90Cl	90	$\text{CoCl}_2 \cdot 6\text{H}_2\text{O}$
S90N	90	$\text{Co}(\text{NO}_3)_2 \cdot 6\text{H}_2\text{O}$

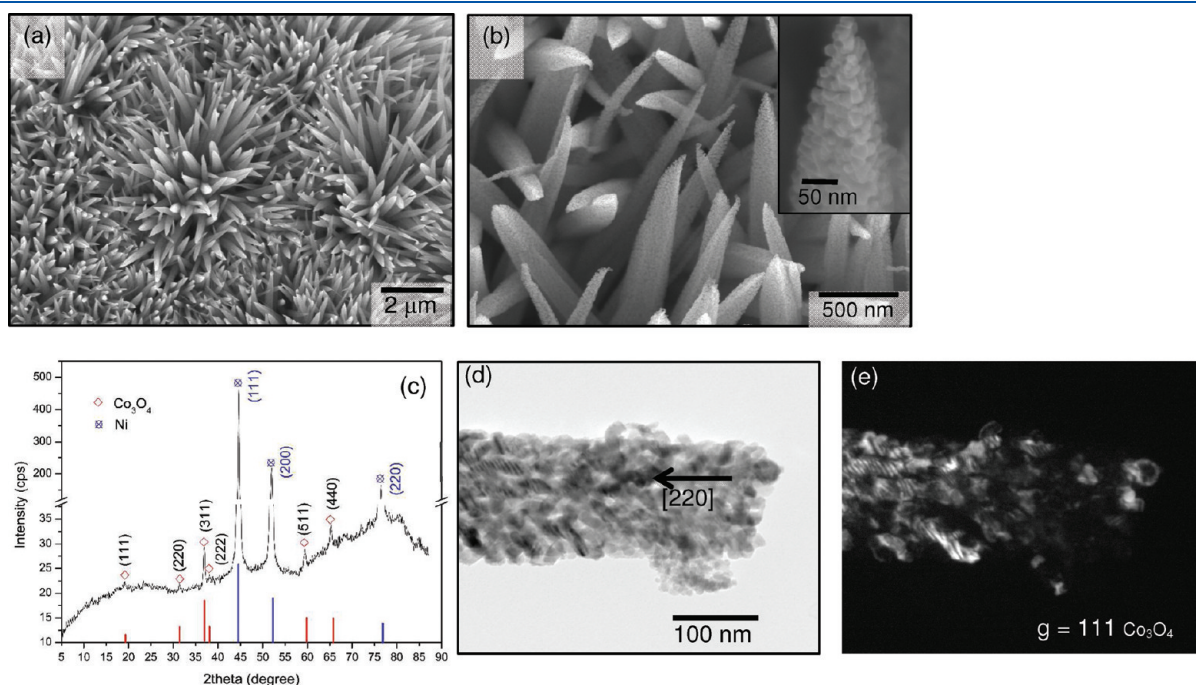


Figure 1. (a),(b) SEM micrographs of the lath Co_3O_4 nanostructures achieved for S90Cl. (c) Indexed XRD pattern of S90Cl on Ni foam. (d),(e) Bright field and dark field TEM micrographs of a fractured section of a single lath highlighting its strong texture and fast $[220]$ type growth direction.

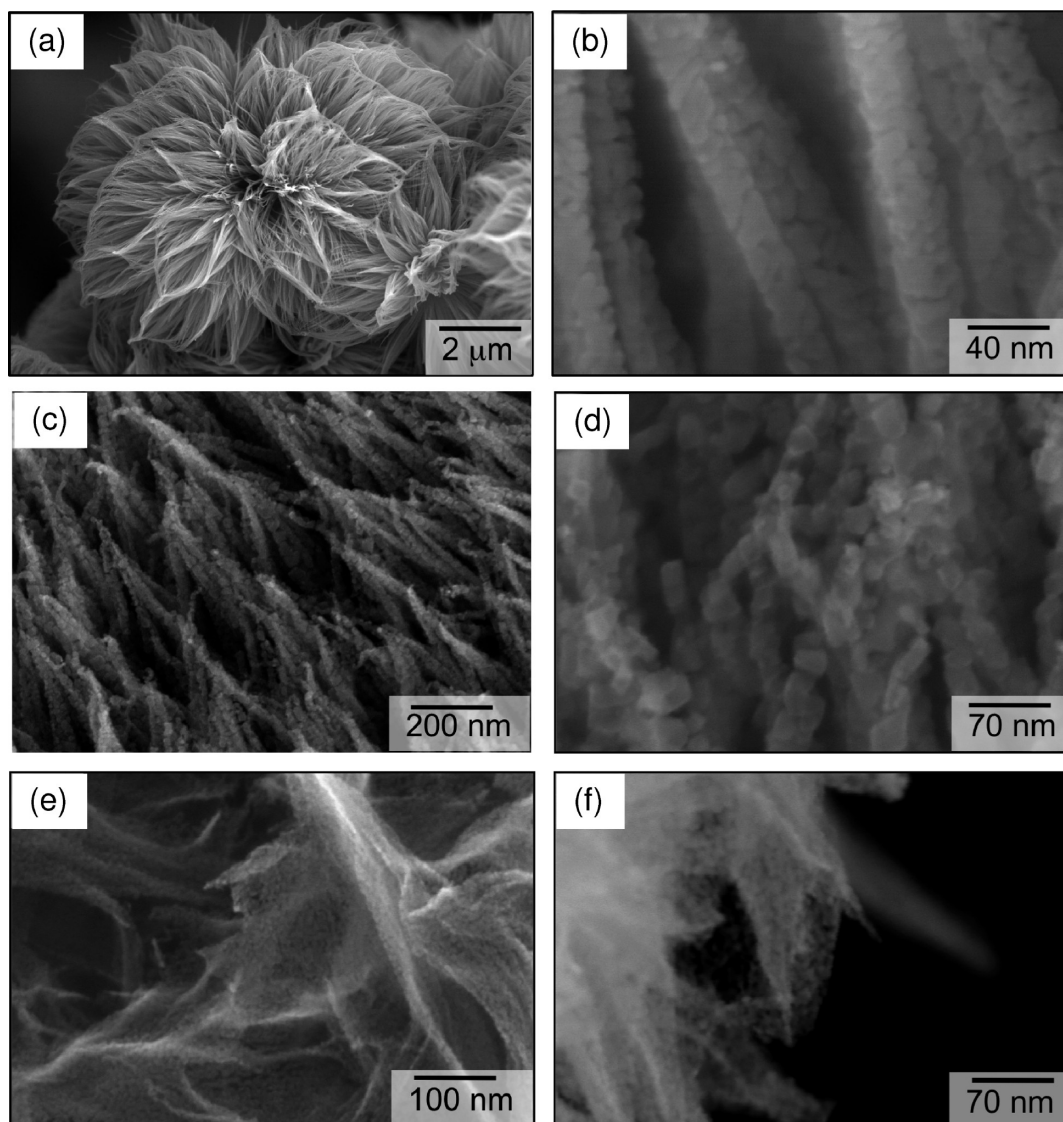


Figure 2. SEM micrographs, shown in order of increasing magnification, of parts (a),(b) “flower” Co₃O₄ nanostructures achieved for S90N. (c),(d) “Necklace” Co₃O₄ nanostructures achieved for S70Cl. (e),(f) “Net” Co₃O₄ nanostructures achieved for S50Cl.

2.2. Microstructural Analysis. A Hitachi S-4800 field emission scanning electron microscope (SEM) and JEOL 2100 and 2010 transmission electron microscopes (TEM) were used to study the sample morphology and structure. Electron diffraction pattern simulation was performed via the commercial software Desktop Microscopist, with the input of the well-known space group information for Co₃O₄. The phases present were also identified using X-ray diffraction (Bruker AXS D8 Discover diffractometer with a GADDS area detector).

2.3. Electrochemical Characterization. For electrochemical testing, the battery grade nickel foam was used as the substrate. Mass quantities of 0.2–20 mg of Co₃O₄ were deposited onto battery grade nickel foam with dimensions of 2 × 10 × 10 mm. The specific capacitance was calculated by dividing the measured capacitance by the corresponding mass loading. The Co₃O₄ covered nickel foams were directly employed as the working electrodes without any polymer binder or conductive additives.

The electrochemical performance of the samples was evaluated on a Princeton applied research workstation (model 616 RDE)

by cyclic voltammetry and charge–discharge tests using a three-electrode cell with Pt foil as the counter electrode and Hg/HgO as the reference electrode. All electrochemical measurements were carried out in 1 M NaOH (analytic grade, Fisher Scientific) at room temperature.

3. RESULTS AND DISCUSSION

3.1. Microstructure. The precalcined samples were identified as cobalt-chloride-hydroxide-carbonate (XRD pattern not shown) [Co(CO₃)_{0.35}Cl_{0.20}(OH)_{1.10}·1.74H₂O, JCPDS Card: 38–0547]. Subsequent calcination in air converted the cobalt-chloride-hydroxide-carbonate into to cubic Co₃O₄ (Fd3m, No. 227). The morphology of the calcined S90Cl specimen, as obtained by SEM analysis, is shown in Figure 1(a),(b). At the 90 °C hydrothermal processing condition, the Co₃O₄ is “lath-shaped”, with the laths consisting of interconnected nanocrystallites. The crystallites varied in scale from 18 to 28 nm, with a mean diameter of 23 nm. Figure 1(c) shows the XRD pattern of

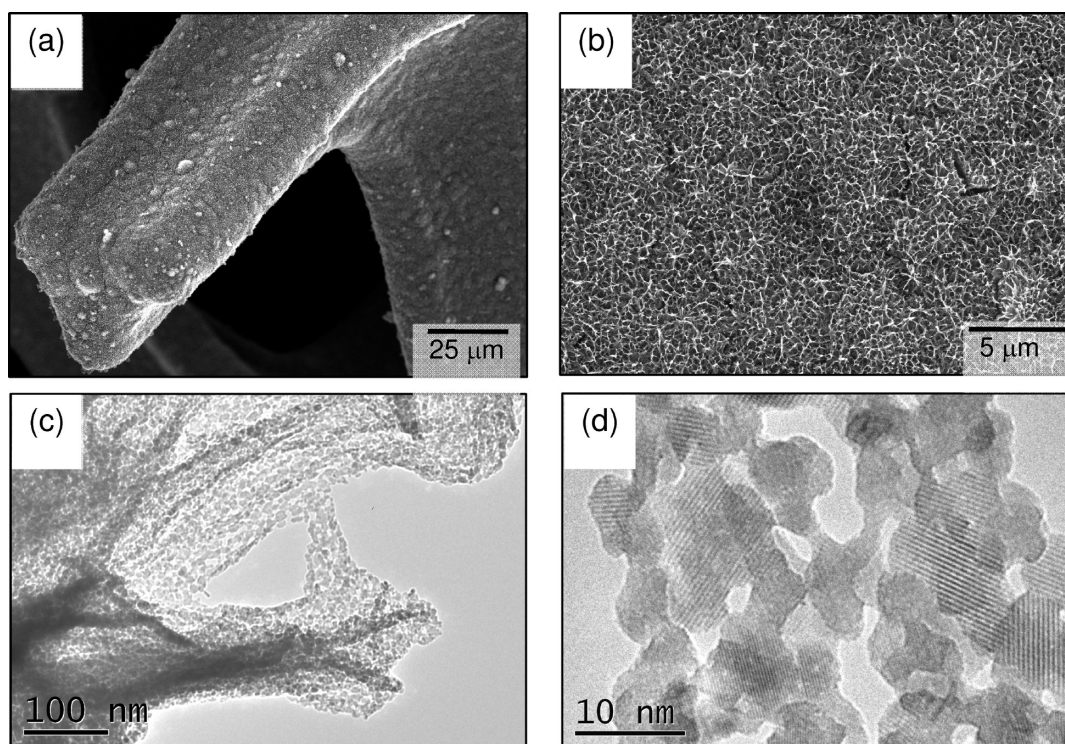


Figure 3. (a),(b) SEM and (c),(d) TEM micrographs of the “net” Co_3O_4 nanostructures achieved for S50Cl. Images shown in order of increasing magnification.

the laths grown on Ni foil, confirming the cubic structure of the oxide. The reflections from the underlying Ni are also visible in the pattern.

Figure 1(d),(e) show representative bright field and dark field TEM micrographs of a section of one of the laths. The bright field image confirms the presence of porosity within the lath. The dark field micrograph shows that the nanocrystallites are heavily textured, having a common orientation relative to the $[220]$ type fast growth direction. Judging from this and from other TEM dark field images, as well as from the accompanying selected area diffraction patterns (not shown), we can conclude that the majority of the crystallites are in the same zone axis. For example in the sample shown, almost the entire lath can be imaged in dark field using $g = 111$ Co_3O_4 . It is known that the formation of porosity during the calcination treatment is mainly induced by the elimination of hydroxyl and carbonate groups during the thermal decomposition.⁴²

The morphology of the as-synthesized Co_3O_4 structures can be tuned by controlling the cobalt precursors and the growth conditions. For example, as shown in Figure 2(a),(b), “flower-like” Co_3O_4 structures (S90N) were synthesized at 90°C by using $\text{Co}(\text{NO}_3)_2 \cdot 6\text{H}_2\text{O}$ as cobalt source. Each flower-like structure is composed of hundreds of nanorods. Every nanorod is $2\text{--}4\ \mu\text{m}$ in length. The nanorods contain porosity between them, and are composed of crystallites having a range of $14\text{--}28\ \text{nm}$ a mean diameter of $21\ \text{nm}$. The different morphology of Co_3O_4 nanostructures grown at 90°C using $\text{CoCl}_2 \cdot 6\text{H}_2\text{O}$ and $\text{Co}(\text{NO}_3)_2 \cdot 6\text{H}_2\text{O}$ as cobalt sources is likely attributed to the unique space-structure of Cl^- and NO_3^- in solution, similarly to what was reported in ref 41.

For the case of $\text{CoCl}_2 \cdot 6\text{H}_2\text{O}$ as the cobalt source, the variation in the reaction temperature plays a crucial role in determining the

morphology and the dimensions of the Co_3O_4 nanostructures. At 70°C , the nanorod arrays adopt a “necklace-like” morphology, as shown in Figure 2(c),(d). Again the nanorods are composed of interconnected nanocrystallites that are roughly of the same scale as those grown at 90°C , with nanocrystalline diameters ranging from $18\text{--}28\ \text{nm}$ with a mean diameter of $22\ \text{nm}$. What really changes however is the number of nanocrystallites that makes up each structure. The laths shown in Figure 1 are at least $200\ \text{nm}$ thick, which means many of the nanocrystallites on the interior of the structure are in contact with the electrolyte only if there is adjacent porosity. In the case of the S70Cl samples, the nanorods are sub- $50\ \text{nm}$ in diameter, giving improved access of the electrolyte to the Co_3O_4 surfaces.

As will be demonstrated in the following section, the S50Cl sample has the best electrochemical performance. We therefore will provide a more detailed description of its microstructure. Figure 2(e),(f) presents SEM micrographs of the “net-like” microstructure of the S50Cl, shown at a comparable scale to the other specimens. As may be seen from the images, the scale of the net-like microstructure is significantly finer than that of samples synthesized at higher temperatures. Shown at the same magnification as the S70Cl, the nanocrystallites in the S50Cl are not visible. Figure 3 further highlights the S50Cl microstructure. The low magnification images shown in Figure 3(a),(b) demonstrate that the Co_3O_4 conformally and uniformly coats the Ni foam surface. Figure 3(a) highlights how well the oxide coats the macroscopically curved Ni foam surface. Though some cracking in the Co_3O_4 layer is visible at higher magnifications, Figure 3(b), it can be safely assumed that the relative fraction of the Ni that is exposed to the electrolyte compared to the oxide is negligible. In other words, one can safely argue that by far the vast majority of the contribution to the faradaic supercapacitance originates from

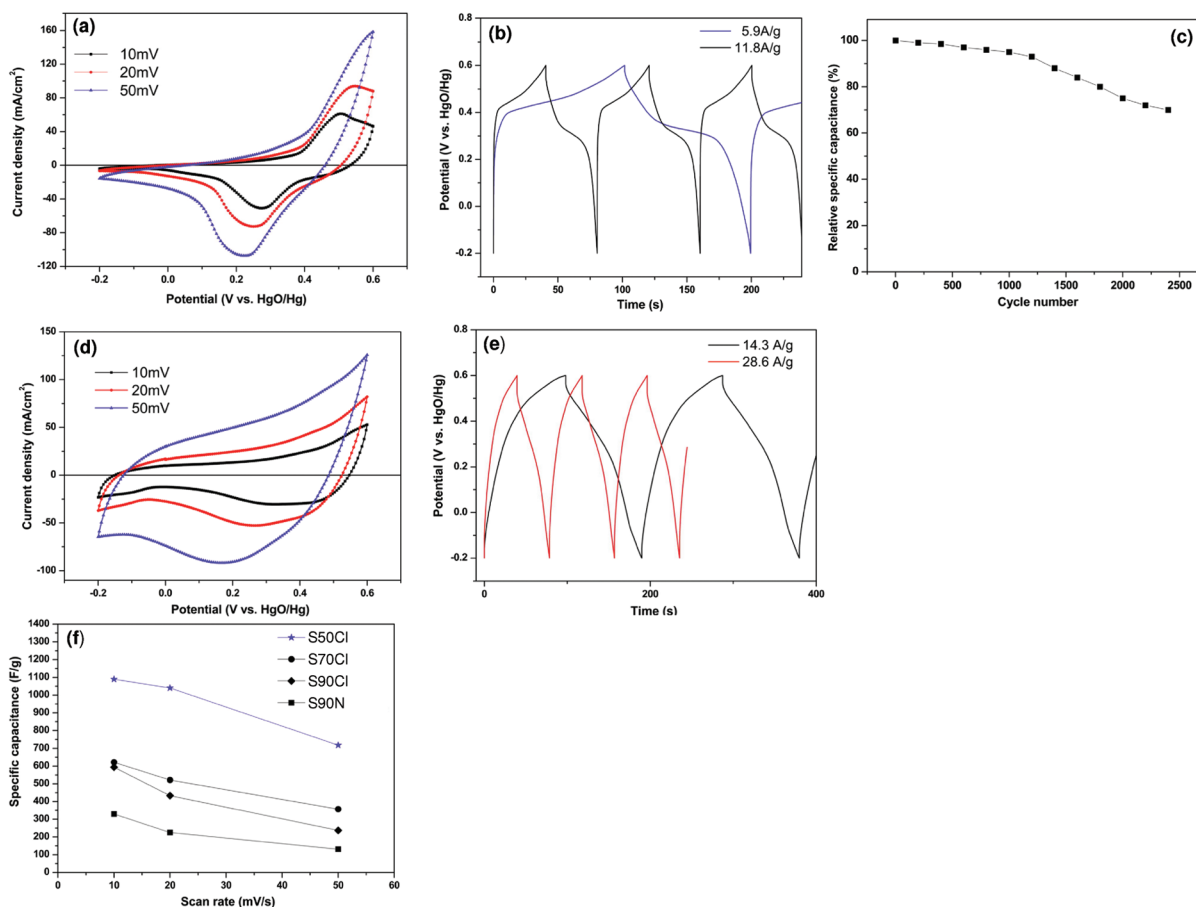


Figure 4. Electrochemical performance: (a) S90Cl cyclic voltammograms (CV), (b) charge–discharge curves, and (c) specific capacitance as a function of current density. (d) S50Cl cyclic voltammograms (CV) and (e) charge–discharge curves. (f) Capacitance for all samples vs scan rate.

the Co_3O_4 rather than from the underlying Ni. Figure 3(c),(d) presents TEM micrographs of the Co_3O_4 structure, shown in order of increasing magnification. The Co_3O_4 nanocrystallites are much finer in scale relative to their dimensions at other processing conditions. Their scale ranges from 5 to 12 nm, with a mean diameter of 8 nm. The nanostructures are highly porous, with the porosity being on the same scale as the crystallite sizes. As will be demonstrated in the next section of the manuscript, such a microstructure yields an exquisite supercapacitive performance.

During calcination, the transformation of the intermediate precursor to the final cobalt oxide (Co_3O_4) is known to be topotactic, with the final oxide nanostructure inheriting the morphology and scale of the intermediate phase.⁴¹ In turn, it is known that the morphology of cobalt-based intermediate nanostructures are strongly determined by the relative concentration of Co^{2+} , HCO_3^{2-} , and OH^- in reaction solution. As we demonstrated in this work, for a given relative concentration of precursors (i.e., relative concentration of ionic species in solution), the reaction temperature makes a profound difference. The refinement of the microstructural scale with decreasing temperature may be explained by classic nucleation and growth theory. At lower temperature, there is a much higher driving force for nucleation and a smaller thermodynamically stable critical nucleus. Meanwhile, the ionic diffusivity is reduced. Both effects lead to finer and more densely distributed intermediate nanostructures at lower hydrothermal synthesis temperatures. It is evident by comparing the “net” morphology achieved at 50 °C versus the

“flower” morphology achieved at 90 °C. The secondary mesoporosity may be attributed to Kirkendall voids formed by fast outward movement of ions during the calcining process. The 50 °C net nanostructures have the highest surface to volume ratio of all the structures synthesized, which results in better electrolyte accessibility to the mesopores.

During the hydrothermal synthesis process, the nickel support will be passivated with a strong nanoscale oxide. Such a surface should serve as an ideal heterogeneous nucleation site for the intermediate nanostructures, as is demonstrated by their 100% preferred growth on the Ni foam versus on the Teflon-coated vessel surface itself.

3.2. Electrochemical Properties. The supercapacitive performance of various as-synthesized Co_3O_4 nanostructures grown on Ni foam was evaluated by cyclic voltammetry (CV) and constant current charge–discharge cycling (CD). The specific capacitance (SC), in Faradays per gram, based on CV and CD cycling can be calculated by the following equations:

$$SC_{CV} = \frac{Q}{m\Delta E} \quad (1)$$

$$SC_{CD} = \frac{i\Delta t}{m\Delta E} \quad (2)$$

where Q is the integrated cathodic (or anodic) charge, ΔE is the potential window, i is the discharge (or charge) current, Δt is the

discharge time, and m is the mass of the supercapacitive material. All SC values were calculated by averaging the capacitance of symmetric anodic and cathodic halves. In all of the electrochemical tests, the mass loading of Co_3O_4 was in the 1.0–1.5 mg/cm^2 range. Authors recently reported that at low mass loadings, i.e., when there is a large fraction of underlying Ni foam that is exposed to the electrolyte, substantial errors in the capacitance calculation may result.⁴³ Since the Co_3O_4 conformally covered the Ni foam and had a relatively high mass loading, the electrochemical contribution from the foam itself should be negligible.

Representative cyclic voltammograms (CV), constant current charge–discharge cycling results, and the specific capacitance versus cycle number (presented as % of the cycle 1 value) for S90Cl are shown in Figure 4(a)–(c). It can be clearly found that there is a distinct pair of redox peaks during the anodic and cathodic sweeps. The shape of the CV curves agrees with previous studies on Co_3O_4 in KOH solution.⁴⁴ The redox peaks correspond to the conversion between different cobalt oxidation states. In the case of oxidation, the two sequential reactions are described as follows:^{45,46}

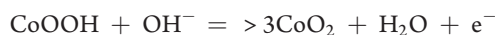


Figure 4(b) shows the constant current charging/discharging behavior at the rates of 5.9 and 11.8 A/g. The curves deviate from the ideal triangular geometry, rather possessing two regions with distinct slopes (albeit both rounded). The fact that the curves are not straight but appear to have a curvature is attributable to the domination of faradaic redox reactions, rather than electrical double layer charging.⁴⁷ The change in the slope in the charging curves at the higher voltage (~ 0.4 V) as well as its asymmetric behavior may be attributed to a high internal resistance of the Co_3O_4 laths. Figure 4(c) shows the cycling stability of the S90Cl lath-like Co_3O_4 nanostructures. The samples were fully charged up to 2500 times, showing roughly a 30% drop in their specific capacitance. Such behavior is appropriate for the Co_3O_4 system, which is known to degrade with cycling.

The S50Cl sample had a tremendous increase in its capacitive behavior as compared to the S90Cl. Figure 4(d),(e) show the CV curves and the charge discharge curves for this material, respectively. For roughly the same mass loading, the CV curves show a much larger area indicating higher levels of stored charge. Meanwhile, the constant current charge discharge curves are more symmetrical, highlighting reduced internal resistance of the material. As discussed in the Microstructure portion of the manuscript the electrochemical improvement may be attributable to the unique open and truly nanoscale structure of the Co_3O_4 “nets”. As compared to the S90Cl laths and other structures, in the S50Cl samples the surface to volume ratio is the highest. Furthermore, due to the fine size of both the columns and of the individual nanocrystallites that constitute them, the electrical path is shorter than in the much thicker structures achieved at higher temperatures. Figure 4(f) summarizes the supercapacitive properties achieved for every growth condition, showing the results as a function of scan rate. Figure 4(f) supports the above argument that lower synthesis temperatures lead to more favorable microstructures for faradaic charge storage.

4. CONCLUSIONS

We have shown that the microstructure of Co_3O_4 may be tremendously influenced through the selection of the appropriate hydrothermal synthesis temperature. This microstructure, in turn, has a profound effect of the supercapacitive performance of the material. At the highest synthesis temperature of 90 °C, the Co_3O_4 structures consisted of polycrystalline laths up to several hundred nanometers in diameter, micrometers in length, and with minor levels of nanoporosity. At a mass loading of 1–1.5 mg/cm^2 , these structures had the worst supercapacitive performance, with values ranging from 340 to 120 F/g, depending on the scan rate. At the lowest synthesis temperature of 50 °C, the Co_3O_4 structures were composed of a highly porous nanoscale net with an average crystallite size of 8 nm and with pore dimensions of similar magnitude. This material possessed excellent supercapacitance at the same high mass loading of 1.4 mg/cm^2 with a specific capacitance of 1090 F/g at a 10 mV/s scan rate. At 1.4 mg/cm^2 , the nets had a specific capacitance of 1090 F/g at 10 mV/s scan rate.

AUTHOR INFORMATION

Corresponding Author

*E-mail: dmitlin@ualberta.ca (D.M.); lzhang12@ualberta.ca (L.Z.).

ACKNOWLEDGMENT

The authors acknowledge the financial support of NINT NRC and NSERC Discovery.

REFERENCES

- (1) Sivakkumar, S. R.; Nerkar, J. Y.; Pandolfo, A. G. *Electrochim. Acta* **2010**, *55*, 3330–3335.
- (2) Pandolfo, A. G.; Wilson, G. J.; Huynh, T. D.; Hollenkamp, A. F. *Fuel Cells* **2010**, *10*, 856–864.
- (3) Algharaibeh, Z.; Pickup, P. G. *Electrochem. Commun.* **2011**, *13*, 147–149.
- (4) Laforgue, A. J. *Power Sources* **2011**, *196*, 559–564.
- (5) Wang, Y. H.; Zhitomirsky, I. *Colloids Surf., A* **2010**, *369*, 211–217.
- (6) Wang, K. X.; Wang, Y. G.; Wang, Y. R.; Hosono, E.; Zhou, H. S. *J. Phys. Chem. C* **2009**, *113*, 1093–1097.
- (7) Wang, Y. T.; Lu, A. H.; Zhang, H. L.; Li, W. C. *J. Phys. Chem. C* **2011**, *115*, 5413–5421.
- (8) Li, J.; Yang, Q. M.; Zhitomirsky, I. *Nanoscale Res. Lett.* **2010**, *5*, 512–517.
- (9) Liu, X. R.; Huber, T. A.; Kopac, M. C.; Pickup, P. G. *Electrochim. Acta* **2009**, *54*, 7141–7147.
- (10) Chen, Y. L.; Hu, Z. A.; Chang, Y. Q.; Wang, H. W.; Zhang, Z. Y.; Yang, Y. Y.; Wu, H. Y. *J. Phys. Chem. C* **2011**, *115*, 2563–2571.
- (11) Donne, S. W.; Hollenkamp, A. F.; Jones, B. C. *J. Power Sources* **2010**, *195*, 367–373.
- (12) Zhang, J. T.; Ma, J. Z.; Zhang, L. L.; Guo, P. Z.; Jiang, J. W.; Zhao, X. S. *J. Phys. Chem. C* **2010**, *114*, 13608–13613.
- (13) Liu, J. W.; Essner, J.; Li, J. *Chem. Mater.* **2010**, *22*, 5022–5030.
- (14) Brezesinski, T.; Wang, J.; Tolbert, S. H.; Dunn, B. *Nat. Mater.* **2010**, *9*, 146–151.
- (15) Zheng, F. L.; Li, G. R.; Ou, Y. N.; Wang, Z. L.; Su, C. Y.; Tong, Y. X. *Chem. Commun.* **2010**, *46*, 5021–5023.
- (16) Cao, L.; Xu, F.; Liang, Y. Y.; Li, H. L. *Adv. Mater.* **2004**, *16*, 1853–1857.
- (17) Liang, Y. Y.; Schwab, M. G.; Zhi, L. J.; Mugnaioli, E.; Kolb, U.; Feng, X. L.; Mullen, K. J. *Am. Chem. Soc.* **2010**, *132*, 15030–15037.
- (18) Zhu, T.; Chen, J. S.; Lou, X. W. *J. Mater. Chem.* **2010**, *20*, 7015–7020.

- (19) Chen, S. Q.; Wang, Y. *J. Mater. Chem.* **2010**, *20*, 9735–9739.
- (20) Zheng, J.; Liu, J.; Lv, D. P.; Kuang, Q.; Jiang, Z. Y.; Xie, Z. X.; Huang, R. B.; Zheng, L. S. *J. Solid State Chem.* **2010**, *183*, 600–605.
- (21) Wang, X.; Wu, X. L.; Guo, Y. G.; Zhong, Y. T.; Cao, X. Q.; Ma, Y.; Yao, J. N. *Adv. Funct. Mater.* **2010**, *20*, 1680–1686.
- (22) Gao, Y. Y.; Chen, S. L.; Cao, D. X.; Wang, G. L.; Yin, J. L. *J. Power Sources* **2010**, *195*, 1757–1760.
- (23) Wei, T. Y.; Chen, C. H.; Chang, K. H.; Lu, S. Y.; Hu, C. C. *Chem. Mater.* **2009**, *21*, 3228–3233.
- (24) Zheng, M. B.; Cao, J.; Liao, S. T.; Liu, J. S.; Chen, H. Q.; Zhao, Y.; Dai, W. J.; Ji, G. B.; Cao, J. M.; Tao, J. *J. Phys. Chem. C* **2009**, *113*, 3887–3894.
- (25) He, L.; Li, Z. C.; Zhang, Z. J. *Nanotechnology* **2008**, *19*, 155606.
- (26) Li, Y. G.; Tan, B.; Wu, Y. Y. *Nano Lett.* **2008**, *8*, 265–270.
- (27) Yu, R. J.; Tao, P. F.; Zhou, X. S.; Fang, Y. P. *J. Alloys Compd.* **2008**, *461*, 574–578.
- (28) Li, W. Y.; Xu, L. N.; Chen, J. *Adv. Funct. Mater.* **2005**, *15*, 851–857.
- (29) Liang, H. Y.; Raitano, J. M.; Zhang, L. H.; Chan, S. W. *Chem. Commun.* **2009**, 7569–7571.
- (30) Feng, J.; Zeng, H. C. *Chem. Mater.* **2003**, *15*, 2829–2835.
- (31) Lou, X. W.; Deng, D.; Lee, J. Y.; Archer, L. A. *J. Mater. Chem.* **2008**, *18*, 4397–4401.
- (32) Shao, Y. Z.; Sun, J.; Gao, L. *J. Phys. Chem. C* **2009**, *113*, 6566–6572.
- (33) Yang, J.; Liu, H. W.; Martens, W. N.; Frost, R. L. *J. Phys. Chem. C* **2010**, *114*, 111–119.
- (34) He, T.; Chen, D. R.; Jiao, X. L.; Xu, Y. Y.; Gu, Y. X. *Langmuir* **2004**, *20*, 8404–8408.
- (35) He, T.; Chen, D. R.; Jiao, X. L.; Wang, Y. L. *Adv. Mater.* **2006**, *18*, 1078–1082.
- (36) Lu, Y.; Wang, Y.; Zou, Y.; Jiao, Z.; Zhao, B.; He, Y.; Wu, M. *Electrochem. Commun.* **2010**, *12*, 101–105.
- (37) Yang, S. B.; Cui, G. L.; Pang, S. P.; Cao, Q.; Kolb, U.; Feng, X. L.; Maier, J.; Mullen, K. *ChemSuschem* **2010**, *3*, 236–239.
- (38) Keng, P. Y.; Kim, B. Y.; Shim, I. B.; Sahoo, R.; Veneman, P. E.; Armstrong, N. R.; Yoo, H.; Pemberton, J. E.; Bull, M. M.; Griebel, J. J.; Ratcliff, E. L.; Nebesny, K. G.; Pyun, J. *ACS Nano* **2009**, *3*, 3143–3157.
- (39) Wang, Z.; Chen, X.; Zhang, M.; Qian, Y. *Solid State Sci.* **2005**, *7*, 13–15.
- (40) Zhang, Y.; Chen, Y.; Wang, T.; Zhou, J.; Zhao, Y. *Microporous Mesoporous Mater.* **2008**, *114*, 257–261.
- (41) Xu, R.; Zeng, H. C. *J. Phys. Chem. B* **2003**, *107*, 12643–12649.
- (42) Tian, L.; Zou, H. L.; Fu, J. X.; Yang, X. F.; Wang, Y.; Guo, H. L.; Fu, X. H.; Liang, C. L.; Wu, M. M.; Shen, P. K.; Gao, Q. M. *Adv. Funct. Mater.* **2009**, *20*, 617–623.
- (43) Xing, W.; Qiao, S.; Wu, X.; Gao, X.; Zhou, J.; Zhuo, S.; Hartono, S. B.; Hulicova-Jurcakova, D. *J. Power Sources* **2011**, *196*, 4123–4127.
- (44) Gao, Y.; Chen, S.; Cao, D.; Wang, G.; Yin, J. *J. Power Sources* **2010**, *195*, 1757–1760.
- (45) Boggio, R.; Carugati, A.; Trasatti, S. *J. Appl. Electrochem.* **1987**, *17*, 828–840.
- (46) Svegli, F.; Orel, B.; Hutchins, M. G.; Kalcher, K. *J. Electrochem. Soc.* **1996**, *143*, 1532–1539.
- (47) Conway, B. E. In *Electrochemical Supercapacitors: Scientific Fundamentals and Technological Applications*; Kluwer Academic/Plenum Press: New York, 1999.